Two-dimensional optics : diffraction and dispersion of surface plasmons

Chimento, P.F.

7
Enhancing the anomalous surface plasmon dispersion in aluminum

The effective index of the surface plasmon mode an an aluminum surface has a region of anomalous dispersion in the near-infrared as a consequence of aluminum's parallel-band transition at 1.5 eV. By cooling aluminum to 86 K and performing surface plasmon resonance experiments in the Otto configuration, we demonstrate a sizeable enhancement of this anomalous dispersion. The second-order dispersion parameter derived from our measurements increases from its room temperature value of 9000 ps/nm·km to 25000 ps/nm·km.

7.1 Introduction

It is widely appreciated that aluminum is a good approximation to a free-electron metal. Aluminum is also eminently suitable for use in plasmonic applications at wavelengths shorter than 600 nm, where gold's absorption starts to be a hindrance.[1] However, aluminum has some surprising properties in the vicinity of its absorption peak around $\lambda \approx 800$ nm. In chapter 6, we reported anomalous dispersion of the surface plasmon mode on an aluminum interface, exploiting this absorption. This feature is unusual, since the dispersion of the surface plasmon mode is usually normal, a consequence of the Drude-like behavior of most plasmonic metals.

[1] West et al., 2010.

Aluminum's absorption peak manifests most visibly as a reflectance dip familiar to anyone who has used aluminum mirrors, and it is due to a parallel-band transition at 1.5 eV.[2] More accurate analysis turned up another parallel-band transition at 0.5 eV ($\lambda \approx 2500$ nm),[3] which had gone undiscovered until then because the Drude-like absorption dominates at that point. Shortly after the latter work, Ashcroft and Sturm developed a theoretical model for aluminum's parallel-band transitions, and pointed

[2] Ehrenreich et al., 1963.

[3] Bos and Lynch, 1970.

out that parallel bands in the vicinity of the {200} set of crystal planes cause the 1.5 eV absorption peak, and likewise, bands near the {111} planes are responsible for the 0.5 eV peak.[4]

[4] Ashcroft and Sturm, 1971.

Interestingly, the parallel-band absorption peaks in aluminum have a pronounced temperature dependence. When the temperature is reduced, they shift toward slightly higher energies, narrow, and become stronger.[5] A pressure dependence was also discovered: at 30 GPa, both absorption peaks move by almost a whole electron volt toward higher energies.[6] In addition, parallel-band transitions occur only in crystalline aluminum, not in liquid aluminum[7] or in other solid states.[8] After the 1980s, the subject of aluminum's parallel-band transitions seems to have been largely forgotten, but the data are far from buried. They are readily available in Palik's well-known *Handbook of Optical Constants of Solids*.[9]

[5] Liljenvall et al., 1971; Mathewson and Myers, 1972; Benbow and Lynch, 1975.

[6] Tups and Syassen, 1984.

[7] Miller, 1969.

[8] Bernland, Hunderi, and Myers, 1973.

[9] Smith et al., 1985.

In this chapter, we present experimental measurements of the temperature-dependent surface plasmon dispersion relation in aluminum in the neighborhood of the resonance at 1.5 eV, using the method of attenuated total reflection in the Otto configuration. We cool the aluminum to liquid-nitrogen temperatures, causing a giant increase in the anomalous dispersion that accompanies the resonance, compared to what we reported in chapter 6. Finally, we discuss the feasibility of surface plasmon solitons on a liquid nitrogen-cooled aluminum surface.

7.2 Temperature dependence of the parallel-band absorption

THE 1960S AND 1970S saw a considerable amount of labor expended on measuring and understanding the optical properties of metallic aluminum. Much of that work was focused on the energy range below 2.5 eV, where interband absorption plays an important role. Work by several authors[10] provided a reasonably accurate description of the interband features and their impact on the optical properties, in particular the interband feature at 1.5 eV. The picture that arose is that most of the interband absorption is due to aluminum's parallel bands near the Fermi energy.[11]

[10] Bennett et al., 1963; Ehrenreich et al., 1963; Dresselhaus, Dresselhaus, and Beaglehole, 1971.

[11] Harrison, 1966.

In 1971, building on this work, Ashcroft and Sturm proposed a more detailed description of the intraband and interband absorption[12] which was in good agreement with experimental data over a relatively large range of energies. Moreover, it allowed them to predict a temperature dependence of the interband absorption peak. Mathewson and Myers[13] employed this theoretical model to analyze the optical constants of metallic aluminum over a wide range of energies, at various temperatures, work which was extended by Benbow and Lynch.[14]

[12] Ashcroft and Sturm, 1971.

[13] Mathewson and Myers, 1972.

[14] Benbow and Lynch, 1975.

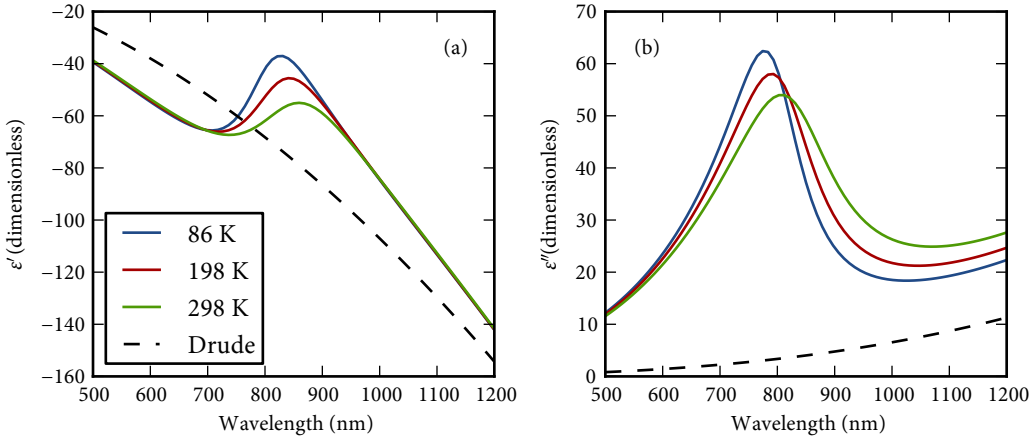

Figure 7.1: Real (a) and imaginary (b) parts of the dielectric function of aluminum, calculated using the model of Ashcroft and Sturm (1971) with temperature-dependent parameters extrapolated from the experimental results of Mathewson and Myers (1972) and Benbow and Lynch (1975). The dashed line is the Drude contribution, without the parallel-band resonance's influence.

Taking the Ashcroft and Sturm model as a starting point, we show the wavelength dependence of the real and imaginary parts of the dielectric function of aluminum in Fig. 7.1. We calculate the curves using parameters derived from Mathewson and Myers, supplemented by data for 4.2 K from Benbow and Lynch. The green (room temperature) and red (198 K) curves correspond to measurements reported in Mathewson and Myers. The blue curve is an estimate, according to the model, of the dielectric function of the aluminum in our liquid nitrogen-cooled experiments at 86 K. The dashed curve shows the Drude contribution to the real and imaginary parts of the dielectric constant. Note that these results suggest that the parallel-band transition's influence can be felt over the whole visible spectrum. While the real part ε' is dominated by the Drude response, the imaginary part ε'' is not.

The resonant feature at $\lambda \approx 850$ nm (1.5 eV) in ε' and ε'' becomes more pronounced as the temperature is reduced. Possibly more important, in particular from the point of view of anomalous dispersion, is that the feature sharpens in both the real and imaginary parts when the temperature is reduced.

7.3 *Experiment*

In order to measure the dispersion relation of the surface plasmon mode on an aluminum surface, we used the method of attenuated total reflection in the Otto configuration,[15] illustrated schematically in Fig. 7.2. The relative merits of the Kretschmann and Otto experimental

[15] Otto, 1968.

configurations have been extensively discussed in chapters 5 and 6; the most important reason for using the Otto configuration is the ability to employ a thick layer of aluminum, with supposedly known optical constants. The thin layers required for the Kretschmann configuration do not always exhibit the parallel-band resonance we are trying to probe,[16] or it is there to a lesser degree.[17]

[16] Novotny, Bulir, et al., 2011.

[17] We have performed preliminary experiments on the low-temperature response of aluminum in a Kretschmann configuration, which also suggest an increase of the anomalous dispersion of the surface plasmon mode.

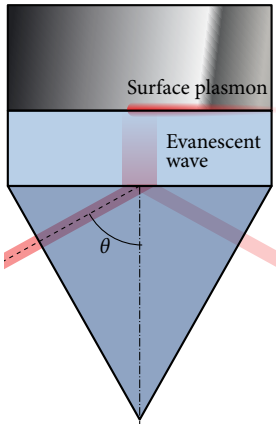

Figure 7.2: The evanescent tail of a light beam, incident in a high-index dielectric (dark blue) at an angle θ greater than the critical angle, excites a surface plasmon on the interface between a metal and a low-index dielectric (light blue).

The Otto configuration involves three materials, a high-index dielectric (dielectric function ε_0), a low-index dielectric (dielectric function ε_1), and a metal (complex dielectric function ε_2, with real part $\varepsilon_2' < 0$). A light beam is incident at an angle θ greater than the critical angle for total internal reflection at the 0–1 interface and undergoes total internal reflection, its evanescent tail extending into medium 1. When the parallel component of the wave vector of the incident beam in medium 0 phase-matches to the surface plasmon mode on the 1–2 interface, then the incident wave can couple to this surface plasmon mode, which is visible as an attenuation of the reflected wave. This evanescent wave coupling is similar to the phenomenon of frustrated total internal reflection.

We used an equilateral prism made of Schott F2 glass ($n \approx 1.608$ at 800 nm) with coatings deposited on all three sides: broadband near-infrared antireflection coatings ($R < 2\%$ for 500–940 nm) on two sides, and three layers on the third side: 570 nm MgF_2 (the low-index dielectric), 100 nm aluminum, and 110 nm SiO_2 as a capping layer to prevent the aluminum from oxidizing.

We placed the prism in a θ–2θ reflectometry setup, already described in chapter 6, and illustrated in Fig. 6.1. This time, the prism was enclosed within a home-built liquid nitrogen bath cryostat. The prism was clamped between two copper cold plates in thermal contact with the liquid nitrogen bath. Monitoring the temperature of the cold plates during the experiment proved them to be stable at 77 K; simulations with the heat flow module of COMSOL suggest that the aluminum layer's temperature reaches a steady state of 86 K within twenty minutes of the cold plates reaching 77 K. The prism assembly was shielded with fiberglass insulation on the sides where optical access was not required, and the entire cryostat was placed on top of the rotation stage of the θ–2θ reflectometer.

As one can see in Fig. 7.1, we need to probe a relatively broad spectral region between approximately 700 and 1000 nm. Therefore, as a light source we used a collimated beam from a fiber-coupled tungsten halogen fiber source (Ocean Optics HL-2000-FHSA-HP), and measured the reflectance spectrum from 620–1000 nm as a function of angle of incidence using a fiber-coupled mini-spectrometer (Ocean Optics USB2000). We

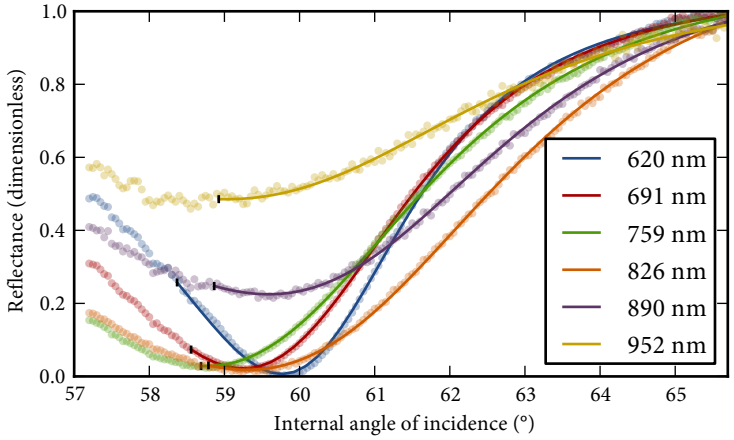

Figure 7.3: Measured reflectance curves for several representative wavelengths. The dots indicate measured values, and the solid lines are fits to the data using (7.1), discussed later in this chapter. The fits cut off at the critical angle for total internal reflection from F2 to MgF_2, where the fit function no longer applies. This is indicated by the small black markers.

show experimental results for selected wavelengths across the wavelength range of interest in Fig. 7.3.

From these measurements we extract the resonance angle by determining the angle at which the reflection reaches a minimum.[18] Figure 7.4 shows the resonance angle as a function of wavelength, for each spectrometer wavelength bin.

[18] For this, we use the minimum of the fitting function (7.1), discussed in the next section.

The resonance angle decreases as a function of wavelength at both long and short wavelengths, as if aluminum were a Drude-like metal in these wavelength ranges. However, the slope of the curve reverses sign in between, and, for the low-temperature curve, the resonance angle increases from about 770 to 870 nm. The data become more noisy at $\lambda > 950$ nm; this reflects the layer thickness getting farther and farther from the thickness necessary for critical coupling. This makes the surface plasmon resonance dip shallower, and its minimum therefore harder to pinpoint exactly.

7.4 *Analysis*

We cannot directly obtain the dispersion of the surface plasmon mode from the results shown in Fig. 7.4, as discussed in chapter 5, since the resonance angle is only an approximate indicator of the surface-plasmon wave vector at a particular wavelength. Therefore, we analyze our angle-dependent wavelength curves using the method outlined in chapter 5 in order to obtain both the real and imaginary parts of the wave vector. We

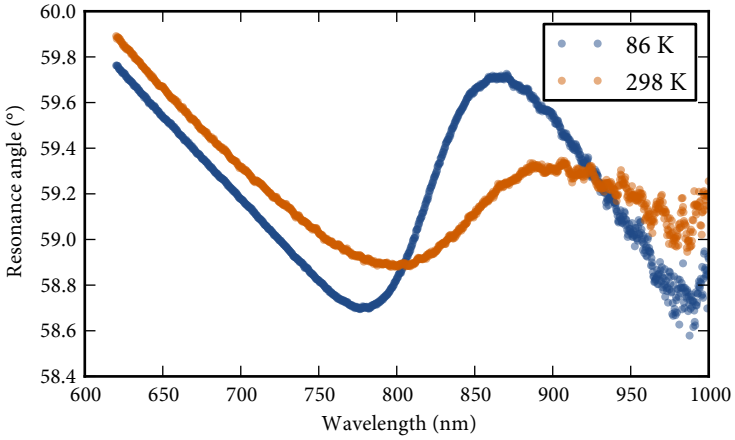

Figure 7.4: Angle of incidence at which the reflectance reaches a minimum, as a function of free-space wavelength. For comparison, we show the same quantity for room temperature (see Fig. 6.6b.)

fit the data with a Fano-type lineshape:

$$R(k_x) = \left| 1 + \frac{A e^{i\phi} k''_{\mathrm{SP}}}{k'_{\mathrm{SP}} + i k''_{\mathrm{SP}} - k_x} \right|^2 , k_x > k_{cr}. \tag{7.1}$$

In this expression, there are four fit parameters: the resonance amplitude A, the phase difference ϕ between the resonance and the background, and the real and imaginary parts of the mode index k'_{SP} and k''_{SP}. We discard the part of the curve measured at angles less than the critical angle, which allows us to set a unit background and fit with only four parameters instead of five as in (5.15). This procedure yields a complex-valued surface plasmon wave vector k_{SP}, and we define the effective surface plasmon mode index to be $n_{\mathrm{SP}} = k_{\mathrm{SP}}/k_0$. This effective mode index is plotted as a function of wavelength in Figure 7.5, where we see a region of anomalous dispersion from about 750 nm to 850 nm, accompanied by an absorption peak centered around 800 nm. The solid lines are the mode index calculated for this system, taking the Ashcroft-Sturm model for the dielectric function of aluminum, as shown in Fig. 7.1. We took as the pseudopotential $U_{200} = 0.795$ eV, as the Drude scattering time $\tau_D = 11.5$ fs, and as the parallel-band scattering time $\tau_I = 6.0$ fs. For the purpose of this calculation, we used a Sellmeier model for the dispersion of F2 glass,[19] MgF_2,[20] and SiO_2.[21] Both the real and imaginary parts of the experimentally determined mode index are slightly higher than the calculated prediction, but exhibit very similar overall behavior.

[19] Schott AG, 2012.
[20] Dodge, 1984.
[21] Malitson, 1965.

Fig. 7.5 demonstrates that the parallel-band absorption resonance in metallic aluminum and its associated anomalous dispersion do indeed influence the dispersion relation of surface plasmons traveling along an

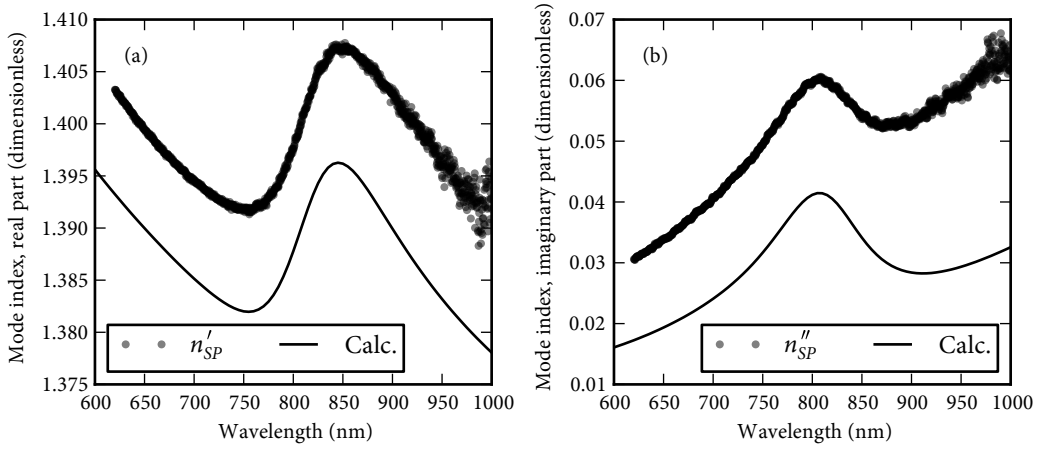

Figure 7.5: Measured real part (a) and imaginary part (b) of the surface plasmon mode index, determined by analysis of the angle-dependent reflectance curves, measured at $T = 86$ K. The solid lines are a calculation of the mode index to be expected for this particular Otto-configuration system, based on the Ashcroft-Sturm model for aluminum's dielectric function and published values for the other materials' optical properties. Compare to Fig. 6.7.

interface between aluminum and a dielectric.

The dispersive features shown in Fig. 7.5 suggest that a short (less than 100 fs) surface plasmon pulse with its center wavelength in the vicinity of the parallel-band absorption will experience substantial pulse reshaping. In order to obtain some insight into the pulse propagation we evaluate the modal group index,

$$n_g = \frac{d\omega}{dk} = n - \lambda \frac{dn}{d\lambda}, \tag{7.2}$$

and the second-order dispersion parameter, which is proportional to the group index's derivative,

$$D = -\frac{\lambda}{c} \frac{d^2 n}{d\lambda^2}. \tag{7.3}$$

In both of the above equations, n refers to the real part of the surface-plasmon mode index. The dispersion is called normal for $D < 0$, and anomalous when $D > 0$.

In order to find the group index and second-order dispersion parameter we smooth the data of Fig. 7.5 using a Savitzky-Golay filter,[22] allowing us to estimate the curves' derivatives. We plot the surface plasmon group index estimated from our data in Fig. 7.6, and for comparison, we also show the group index obtained in the same way from the room-temperature Otto data of chapter 6. We clearly see that a plasmonic pulse would experience strong dispersion in the parallel-band region, which is greatly enhanced by cooling down the aluminum.

[22] Savitzky and Golay, 1964.

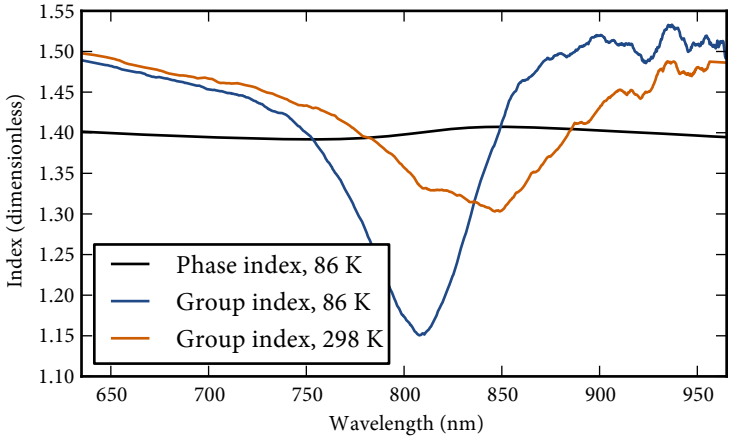

Figure 7.6: Real parts of the group and phase index (smoothed version of Fig. 7.5a) of the surface plasmon mode, as a function of free-space wavelength. For comparison, the same quantity at room temperature is shown (orange), as calculated from the data of chapter 6.

Our estimates for the second-order dispersion parameter D, expressed in ps/nm·km,[23] are shown in Fig. 7.7. At both temperatures, there is a region where D is positive, meaning that the group velocity dispersion is anomalous.

[23] A unit for D common in fiber optics, meaning picosecond delay per nanometer bandwidth and kilometer propagation length.

At the peak of the anomalous dispersion regime, the second-order dispersion reaches the large value of 25000 ps/nm · km. The peak value at room temperature is about 9000 ps/nm · km, meaning that cooling to liquid nitrogen temperatures causes almost a threefold increase of this peak value. The wavelength range in which anomalous dispersion occurs, however, is narrower (about 70 nm versus 100 nm at room temperature.) This is consistent with Mathewson and Myers'[24] earlier measurements demonstrating that the parallel-band resonance became stronger and narrower at lower temperatures.

[24] Mathewson and Myers, 1972.

We now consider using this anomalous dispersion to create a surface plasmon soliton. The anomalous dispersion region is about 70 nm wide, centered around 830 nm. This bandwidth corresponds approximately to a 14 fs Fourier-limited pulse width. Surface plasmons generally have a short decay length, typically less than 50 μm in the relevant wavelength range. The broadening of a 14 fs pulse associated with $D = 25000$ ps/nm · km over a length of 50 μm is 88 fs. However, the $1/e$ surface plasmon amplitude damping length at 830 nm in our measurements is a mere 2.2 μm, leading to a pulse broadening of 3.8 fs over one damping length.

However, this does not mean that a surface plasmon soliton is possible on an unmodified aluminum-vacuum interface. A soliton pulse in

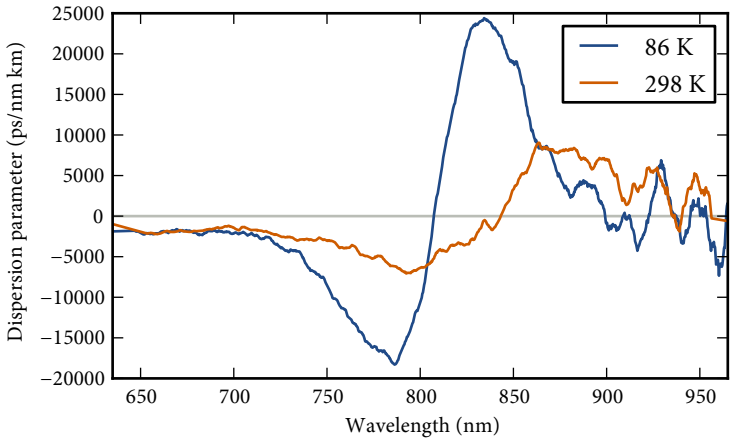

Figure 7.7: Second-order dispersion parameter D estimated from the measured surface plasmon dispersion relation, as a function of free-space wavelength. Note the region where $D > 0$, where the group dispersion is anomalous.

conventional optics requires both anomalous dispersion and Kerr nonlinearity in order to maintain its shape. For a surface plasmon soliton, the aluminum must be paired with a dielectric exhibiting the Kerr effect, changing the dispersion relation. Although Sámson et al.[25] suggest using a pulse with a peak power high enough that the metal's intrinsic Kerr nonlinearity suffices, we suspect that this would prove prohibitively damaging. Huang, Chang, Leung, and Tsai[26] suggest a possible expression for the dispersion relation of a surface plasmon on the interface between an ideal metal and a Kerr medium.

[25] Sámson et al., 2011.

[26] Huang et al., 2009.

The propagation losses are an additional consideration for a surface plasmon soliton. When the $1/e$ amplitude damping length of a surface plasmon is little more than 2 μm, then to be of any use there must be some form of loss compensation added to the surface plasmon mode. Pairing the metal with a pumped gain medium as the dielectric[27] seems a promising way to achieve this.

[27] Noginov et al., 2008.

7.5 *Conclusion*

By cooling aluminum to 86 K, we have demonstrated a sizeable enhancement of the anomalous dispersion in the effective surface plasmon mode index previously reported in chapter 6. The measured dispersion relation indicates that there is a wavelength region between approximately 810 and 880 nm where the second-order dispersion is anomalous, meaning this system is capable of supporting a plasmon soliton, provided that some form of nonlinear Kerr effect can be added and the propagation losses can be compensated.

Appendix 7.A Ashcroft-Sturm model for the temperature-dependent parallel-band conductivity

[28] Ashcroft and Sturm, 1971.

ASHCROFT AND STURM[28] were the first researchers to derive explicit expressions for the contribution to the optical conductivity, and therefore to the dielectric function, from parallel-band transitions. However, their paper unfortunately contains several misprints, making it nearly impossible to use their results simply by reading their paper. In this appendix we hope to correct this state of affairs by reprinting the expressions we obtained by going through their derivation carefully and simplifying the notation here and there.

Ashcroft and Sturm cast their model in the form of the optical conductivity, which describes the metal's optical properties equivalently to the dielectric function ε. They are related as follows:

$$\varepsilon(\omega) = 1 + i\sigma(\omega)/\omega\varepsilon_0. \tag{7.4}$$

The parallel-band model, $\sigma(\omega) = \sigma_D(\omega) + \sigma_I(\omega)$, consists of an interband contribution $\sigma_I(\omega)$ and a free-electron contribution $\sigma_D(\omega)$,

$$\sigma_D(\omega) = \frac{\sigma_{DC}}{1 - i\omega\tau_D}. \tag{7.5}$$

DC: direct current

Equation (7.5) is equivalent to the more familiar form of the Drude model, (5.1), with the Drude electron scattering time $\tau_D = 1/\gamma$ and the DC conductivity $\sigma_{DC} = \varepsilon_0\tau_D\omega_p^2$. The interband contribution takes the form of $\sigma_I(\omega) = \sum_K \sigma_{I,K}(\omega)$, where K is the reciprocal lattice vector corresponding to the set of planes in which the parallel bands occur, and the expression takes the sum over all such sets of planes. The contribution from one set of planes $\sigma_{I,K}(\omega)$ is a complicated expression, but it is governed by the interband electron scattering time τ_I, and the two energies between which parallel-band absorption occurs: the lower bound

$$\hbar\omega_- = 2U_K, \tag{7.6}$$

where U_K is the Fourier component of the pseudopotential for K; and the upper bound

$$\hbar\omega_+ = (\hbar^2K^2/2m_*)(2k_F/K - 1), \tag{7.7}$$

where m_* is the effective optical mass of a conduction electron and k_F is the Fermi wave vector. There is also a "normal" interband contribution to the absorption (i.e. not due to parallel bands) which dominates for $\omega > \omega_+$, but it is negligible within the frequency regime that we are examining.

In short, the model is an integral over a density of states in the portion of k-space in which the parallel-band absorption occurs. The two scattering times τ_D and τ_I are important, because they remove all sorts of influences from the model. For example, the influence of aluminum film thickness discussed in chapter 6 manifests itself as a broadening of the interband scattering, which is why the resonance is less in evidence. Experiments suggest that in rough terms, $\tau_D \approx 2\tau_I$ for any temperature,[29] which suggests that the electron-phonon scattering dominates τ_I.[30] However, in other circumstances, experimental observations suggest that the values of τ_I for resonances associated with different sets of planes diverge, and separate values τ_{200} and τ_{111} are necessary to explain the observed data.[31]

[29] Mathewson and Myers, 1972.

[30] Benbow and Lynch, 1975.

[31] Benbow and Lynch, 1975; Tups and Syassen, 1984.

THE FULL EXPRESSIONS for the real and imaginary parts of the parallel-band conductivity for one set of planes, reproduced from Ashcroft and Sturm in slightly simplified form, are:

$$\sigma(\omega)' = \frac{\sigma_0 z J(\omega)}{\rho(z^2 + b^2)}; \tag{7.8}$$

$$\begin{aligned}\sigma(\omega)'' = \frac{\sigma_0}{2\pi b\rho}\Bigg(&\tfrac{1}{2}\sin\varphi_+ \ln\frac{t_0^2 + 2t_0\rho\cos\varphi_+ + \rho^2}{t_0^2 - 2t_0\rho\cos\varphi_+ + \rho^2} \\ &+ \cos\varphi_+\left(\arctan\frac{t_0 + \rho\cos\varphi_+}{\rho\sin\varphi_+} + \arctan\frac{t_0 - \rho\cos\varphi_+}{\rho\sin\varphi_+}\right) \\ &+ \pi\frac{b^2 - z^2}{b^2 + z^2}J(\omega)\Bigg),\end{aligned} \tag{7.9}$$

where the quantities $z = \omega/\omega_-$, $b = 1/\omega_-\tau_I$, $\rho = \left((1 - b^2 + z^2)^2 + 4z^2b^2\right)^{1/4}$, and $t_0 = \sqrt{\omega_+/\omega_- - 1}$ are all dimensionless and represent frequency ratios, the angles

$$\varphi_\pm = \frac{\pi}{4} \pm \frac{1}{2}\arctan\frac{1 + b^2 - z^2}{2bz}, \tag{7.10}$$

σ_0 is a constant with units of conductivity defined as $e^2 M_K K/24\pi\hbar$ with e the elementary charge and M_K the multiplicity associated with the K set of planes, i.e. how many planes bound the first Brillouin zone: 48 for the {111} set of planes and 24 for the {200} set of planes. (The solid angle wedge defined by the *XULKW* points in the Brillouin zone is one forty-eighth of

the entire zone.) $J(\omega)$ is a complicated real-valued function defined as

$$\begin{aligned}\pi J(\omega) = {} & \frac{4zb\rho}{z^2+b^2}\arctan t_0 \\ & + \frac{1}{2}\left(\frac{z^2-b^2}{z^2+b^2}\cos\varphi_- + \frac{2zb}{z^2+b^2}\sin\varphi_-\right)\ln\frac{t_0^2+2t_0\rho\sin\varphi_-+\rho^2}{t_0^2-2t_0\rho\sin\varphi_-+\rho^2} \\ & + \left(\left(\frac{z^2-b^2}{z^2+b^2}\sin\varphi_- - \frac{2zb}{z^2+b^2}\cos\varphi_-\right)\right. \\ & \left.\times\left(\arctan\frac{t_0+\rho\sin\varphi_-}{\rho\cos\varphi_-} + \arctan\frac{t_0-\rho\sin\varphi_-}{\rho\cos\varphi_-}\right)\right). \end{aligned} \tag{7.11}$$

Contrary to what Ashcroft and Sturm assert on p. 1902, $J(\omega)$ does not tend to unity for $\omega \to \infty$.

In order to gain a little insight into these difficult expressions and to reproduce Ashcroft and Sturm's Figs. 4 and 8, we also consider the expressions for the limit in which there are no electron collisions ($\tau \to \infty$). In this case, $J(\omega)$ reduces to the much simpler

$$J(\omega) = H(\omega-\omega_-) - H(\omega-\omega_+), \tag{7.12}$$

where $H(\omega)$ is the Heaviside step function. It is now apparent that the physical meaning of $J(\omega)$ is simply the frequency range in which parallel-band absorption occurs (ω_- to ω_+): the parallel-band absorption is absent at lower energies, and at higher energies it is replaced by what Ashcroft and Sturm term the "normal" interband absorption, which we shall not cover in this appendix. The complicated expression in which electron collisions are included simply softens the sharp transition between absorption regimes. The real part for the collisionless case is then

$$\sigma(\omega)' = \begin{cases} \frac{\sigma_0}{z\sqrt{z^2-1}}, & \omega_- < \omega < \omega_+, \\ 0, & \text{otherwise}, \end{cases} \tag{7.13}$$

The imaginary part is given by two expressions, one for frequencies below ω_- and one for frequencies above:

$$\sigma(\omega)'' = \begin{cases} \frac{2\sigma_0}{\pi z}\left(\frac{1}{\sqrt{1-z^2}}\arctan\frac{\sqrt{z_0^2-1}}{\sqrt{1-z^2}} - \arctan\sqrt{z_0^2-1}\right), & \omega < \omega_-, \\ \frac{2\sigma_0}{\pi z}\left(\frac{1}{2\sqrt{z^2-1}}\ln\frac{\sqrt{z_0^2-1}-\sqrt{z^2-1}}{\sqrt{z_0^2-1}+\sqrt{z^2-1}} - \arctan\sqrt{z_0^2-1}\right), & \omega > \omega_- \end{cases}, \tag{7.14}$$

where $z_0 = \omega_+/\omega_-$.

Ashcroft and Sturm calculate their figures using values for the scattering times of $\tau_I = \tau_D = 0.6 \times 10^{-14}$ s,[32] pseudopotentials $U_{111} = 0.0179$ Ry (0.244 eV) and $U_{200} = 0.0562$ Ry (0.765 eV),[33] and $a_0 k_F = 0.9247$. We have made our computer code available with which we calculate the conductivity and dielectric function of aluminum.[34]

[32] Ashcroft and Sturm, 1971.

[33] Ashcroft, 1963.

[34] Chimento, 2013a.